Statistical analysis of focused beam radiographs taken from a coaxial airblast spray

J.K. Bothell, D. Li, T.B. Morgan, T.J. Heindel,
Center for Multiphase Flow Research and Education,
Department of Mechanical Engineering, Iowa State University,
Ames, IA, 50011, USA

N. Machicoane, A. Aliseda
Department of Mechanical Engineering,
University of Washington,
Seattle, WA, 98195, USA

A.L. Kastengren
Advanced Photon Source,
Argonne National Laboratory,
Lemont, IL, 60439 USA

Abstract

Studying the near-field region of sprays is particularly challenging because it is optically dense. However, energy in the X-ray range is capable of penetrating this dense region and obtaining information that would otherwise be unavailable. Through time-resolved X-ray radiography, a better understanding of the near-field region is currently being developed. The 7-BM beamline at the Advanced Photon Source at Argonne National Lab was focused down to a 5 x 6 μm cross-sectional area. The attenuation in the beam, which is used to calculate the effective path length of liquid, was then collected at an effective rate of 270 kHz for 10 seconds. Various statistical measures were applied to the X-ray focused beam radiographs including average, standard deviation, skewness, and kurtosis, to quantify the spray from a canonical coaxial airblast nozzle. Results show that the average effective path length is useful in determining the intact length and spray angle. The capabilities of additional statistical measures in determining important spray characteristics are also discussed.

*Corresponding author: jbothell@iastate.edu

Introduction

Coaxial airblast sprays are of interest because of their use as fuel injectors for gas turbines and jet engines, two-phase chemical reactors, spray drying, and food processing [1]. Many past studies of sprays have utilized visual light for phase Doppler anemometry [2], particle image velocimetry [3], and shadowgraphy [4]. However, the near-field region of a spray is difficult to visualize with visible light because the region is optically dense. Recently, X-ray radiography for visualizing and measuring the near-field region of sprays has gained traction [5]. Many of these studies focus on diesel injectors and find properties such as the velocity of diesel being injected [6] and mass accumulation of the diesel fuel [7].

Studies about adding swirl to the air portion of a coaxial spray show that atomization is at the highest value when the swirl ratio (SR) value is around 0.45 [8]. This study uses a synchrotron X-ray beam, focused to a small cross-sectional area and raster scanned across the spray, to take highly time-resolved radiographs. Various statistical metrics of focused beam radiographs bring a novel perspective to the effect of adding swirl to the air portion of a coaxial spray.

Experimental Methods

Experiments were conducted at the 7-BM beamline at the Advanced Photon Source (APS) at Argonne National Laboratory.

APS uses synchrotron technology to provide high energy X-ray photon beams. The electrons move around a storage ring where a series of bending magnets, wigglers, or undulators are used to bend the beam around the ring, creating a tangent beam of radiation at each turn. Experiments described here used the 7-BM beamline at the APS which is currently set up for taking radiographs of sprays. This beamline uses a bending magnet to produce radiation that is then sent through two hutches. 7-BM-A is the first hutch and is where filtering optics work to produce a beam of the desired wavelength. 7BM-B is the second hutch, and is where beam focusing and the experiment is housed. The beamline is in a fixed location, so the experimental flow loop setup (Figure 1) is built around the beamline. The setup of the 7-BM beamline is described in more detail elsewhere [9].

The air inlet used in this setup comes from pressurized building air at APS. It first passes through a filter to ensure that the air supply is clean. The filter also works to partition the air into two lines, each of which has a pressure transducer to limit the air pressure that is fed to the system. One of the lines is partitioned after the pressure transducer into two additional lines, one that feeds the straight co-flow air and another that feeds the swirl air. There is a ball valve on each of the air lines to force the air line closed when it is not in use. Electronic proportioning valves and air flow meters are located after the ball valves and are used to control and monitor the air flow rates. Both of the air lines are split into four lines, after passing through flow meters, that are then attached to the upper portion of the nozzle to provide air flow for the experiments. The four lines that run from the air flow meters to the nozzle are kept at equal lengths and inner diameters (ID) to ensure equal head loss amongst the lines, shown in Figure 1.

After the filter, the other air line is fed into the water tank to create a pressurized section of air on the top of the tank that then provides the force necessary to push the water through the water line. From there, the water moves through a ball valve that is used to close the water line when no tests are being performed. Then the liquid moves through an electronic proportioning valve and water flow meter. Then the line is split into two lines of equal length and ID. The two lines then feed into the two sides of the liquid chamber in the upper portion of the nozzle, shown in Figure 2.

The electronic proportioning valves and flow meters are connected to a data acquisition system that provides real-time measurement and control. The electronic proportioning valves are controlled by an in-house LabVIEW Proportional, Integral, and Derivative (PID) active control system. Values from the flow meters are sent to the data acquisition system and are used as the feedback as well as being stored so that any natural phenomenon can be related to the instantaneous flow measurement. The LabVIEW program has real-time control of the electronic proportioning valves.

The synchrotron beam is filtered so that only a small range of wavelengths exist and focusing mirrors are used to reduce the size of the beam to 4×5 μm before it passes through the spray. Radiographs are then taken by raster scanning across the spray and taking radiographs at multiple x-y locations. After passing through the spray, the beam hits a PIN diode consisting of a p-type semiconductor, an intrinsic semiconductor, and an n-type semiconductor. The diode allows energy to pass through that is proportional to the intensity of the beam. From there, the current is sent to an oscilloscope and finally recorded by a computer. Focused beam radiographs are taken at a rate of 6.25 MHz for 10 seconds and then those radiographs are binned so that the effective data measurement rate is 270 kHz.

The nozzle shown in Figure 2 contains an upper chamber for water and a lower plenum for gas. The water was injected into the chamber through two, 6.35 mm lines that sit at the upper portion of the chamber. The nozzle was designed to produce laminar, swirl-free, and axisymmetric flow. It has a long liquid needle so that by the time the liquid exits, it is fully developed Poiseuille flow. The actual liquid flow inner diameter at the nozzle exit, as measured through X-ray radiographs, was d_l = 2.1 mm and the outer diameter of the liquid nozzle was D_l = 2.7 mm.

Gas is injected into the plenum through eight lines, four of which are 12.7 mm, evenly spaced gas lines, around the shaft of the nozzle. These four gas lines enter the gas plenum pointing towards the water flow axis and perpendicular to the tangent line of the cylindrical shaft. The other four lines are 9.53 mm inlets for swirl air that are evenly spaced around the shaft and in the same plane as the straight air-lines but offset to create rotation about the centerline. The gas contraction region of the nozzle is a cubic spline shape with minimal angle, designed with the capability to produce even flow throughout the nozzle [10]. The inner diameter of the gas stream was d_g = 10 mm.

The results that are obtained directly from focused beam testing provide a time-resolved radiograph of the intensity of the beam. Using Beer-Lambert's law, the effective path length (EPL) is calculated from the intensity of the beam, I for each location as:

$$EPL = \frac{1}{\mu} ln\left(\frac{I_0}{I}\right) \quad (1)$$

where I_0 is the intensity of the beam where it is not passing through any liquid and μ is the attenuation coefficient for the material through which the beam passes (water was used for this study). The EPL is a length measurement of the total liquid length in the beam. For all of the conditions presented, the total liquid flow rate, Q_l = 0.099 LPM, the total gas flow rate, Q_g = 150 LPM were held constant. The ratio of swirled air to straight air (SR) was varied and ranged from SR = 0 (no swirl) or SR = 1 (equal swirl and straight air). The nondimensionalized Reynolds numbers that relate to the total liquid and gas flow rate are Re_l = 21,200 and Re_g = 1,100, respectively. These are found using equations (2) and (3):

$$Re_l = (U_l d_l)/\nu_l \quad (2)$$

In Equation (1), d_l is the inner diameter of the liquid nozzle, ν_l is the kinematic viscosity of water. U_l is the mean exit velocity and is calculated as $U_l = Q_l/A_l$ where Q_l is the liquid flow rate, and A_l is the exit area of the liquid nozzle. Re_g is defined as:

$$Re_g = \frac{4Q_{tot}}{\pi d_{eff}\nu_g} \quad (3)$$

where Q_{tot} is the total gas flow rate, ν_g is the kinematic viscosity of air, and the effective inner diameter of the gas nozzle, d_{eff} is:

$$d_{eff} = \left(d_g^2 - D_l^2\right)^{\frac{1}{2}} \quad (4)$$

Here, D_l is the outer diameter of the liquid nozzle and d_g is the inner diameter of the gas nozzle (d_g = 10 mm).

The average of the focused beam radiographs was calculated as:

$$\overline{EPL} = \frac{1}{n}\sum_{i=1}^{n} EPL_i \quad (5)$$

where n is the number of measurements at a given data location, EPL_i is the instantaneous EPL, and $\overline{EPL}$ is the average EPL. The standard deviation was calculated as:

$$EPL_{SD} = \sqrt{\frac{1}{n-1}\sum_{i=1}^{n}(EPL_i - \overline{EPL})^2} \quad (6)$$

where EPL_{SD} denotes the standard deviation of the EPL. The skewness was calculated as:

$$EPL_{skew} = \frac{\frac{1}{n}\sum_{i=1}^{n}(EPL_i - \overline{EPL})^3}{\left[\frac{1}{n}\sum_{i=1}^{n}(EPL_i - \overline{EPL})^2\right]^{1.5}} \quad (7)$$

where EPL_{skew} is the skewness of the EPL. The kurtosis was calculated as:

$$EPL_{kurt} = \frac{\frac{1}{n}\sum_{i=1}^{n}(EPL_i - \overline{EPL})^4}{\left[\frac{1}{n}\sum_{i=1}^{n}(EPL_i - \overline{EPL})^2\right]^2} \quad (8)$$

where EPL_{kurt} is the kurtosis of the EPL.

Results and Discussion

Focused beam radiographs were taken by raster scanning across the spray. The data point locations are shown in Figure 3. Each circle represents one data point location but is not representative of the beam size as the beam was 4×5 μm.

Figures 4a, b, and c show the average EPL, calculated from radiographs taken by the focused synchrotron X-ray beam. The blocks within the figures represent data from a point located in the center of each block. The nozzle centerline is located at $y/d_l = 0$, and the first row of data are taken at $x/d_l = 0.26$. Successively wider scans were used as the axial distance increased to ensure that the entire spray region was captured.

The average EPL plots shown in Figures 4a, b, and c represent the mass distribution of liquid at each (x, y) location where focused beam radiographs were taken throughout the spray. Average EPL plots are used in determining the spray angle and can be used to estimate the intact length or core length [11]. As the SR increases from 0 to 0.5, the spray angle increases but when the SR is increased further to SR = 1, the spray angle decreases but is still wider than the condition with SR = 0. The core length follows this same pattern, shortening as the SR increases from 0 to 0.5 and then lengthening when the SR is increased to 1 but remaining shorter than the SR = 0 condition.

Standard deviation plots from the same focused beam radiographs are mapped in Figures 4d, e, and f. Comparing Figure 4a to Figure 4d shows that the standard deviation is the greatest in the region surrounding the core. Figure 4b and e follow the same pattern relating the maximum standard deviation to the region surrounding the core in Figure 4c and f, respectively. Videos of the same spray from synchrotron white beam X-ray imaging in [12] give further insight into the increase in standard deviation around the core region. Throughout the videos, the liquid core can be seen oscillating, explaining the high standard deviation at the core edge. Ligaments from the core are also shed periodically, which explains the high standard deviation at the lower portion and just below the core.

The skewness measures of the focused beam radiographs are shown in Figures 4g, h, and i. The color bar scales vary between conditions because of the large difference in maximum values. The skewness plots give good insight into the location of the edge of the spray which is the most evident in Figure 4g where values were taken beyond the edge of the spray and show low skewness values. Beyond showing the edge of the spray, skewness plots provide no additional insight that can be related to physical properties of the spray.

The kurtosis was also calculated from the focused beam radiographs and is shown in Figures 4j, k, and l. The color bar for these three plots varies for each condition because of the difference in maximum kurtosis values. Similar to the skewness, the edge of the spray is evident in kurtosis measurements. However, beyond showing the edge of the spray, kurtosis measurements have yet to give insight into additional spray characteristics.

Using the same data from which the plots in Figure 4a, d, g, and j were created, Figure 5 shows the probability density function (PDF). The portion of the average EPL plot (in Figure 5a) that is boxed is expanded and represented by PDF of EPL plots in Figure 5c. The PDF plots break the sample space, with a range from 0 to 1.3 EPL/d_l, into 52 smaller ranges where each of the small ranges corresponds to a set of values with a range of 0.0255 EPL/d_l. The PDF plots use a square root scale to improve the visibility of smaller intensity values. In Figure 5b, one of the plots is expanded to show the horizontal and vertical scales that are used for all of the plots in Figure 5c.

Figure 5 presents a spray with no swirl in the air, SR = 0. Looking at the region along the center of the spray in Figure 5a shows that for the region very near the nozzle, the EPL/d_l values have a narrow distribution and never present zero values, representing the core of the spray. When the spray progresses further downstream, as shown in the midsection of Figure 5a, the EPL/d_l values become more distributed as the spray goes through initial breakup. Nearing the lower portion of the tested region the EPL/d_l values shift towards smaller values because the spray breaks into small droplets. Moving further away from the center of the spray, the PDF plots in the center two columns of Figure 5c show the spray converging at first, following the outline of the spray core, and then diverging once the core has gone through initial breakup. The PDF plots that are furthest from the center of the spray represent the outer portion of the spray. Near the nozzle, there are only zero values, as the spray is not found in this region. Further downstream, the spray begins to show EPL/d_l values with a relatively small range of lengths, providing evidence that the droplets are similar in size in this region. At the maximum x/d_l location, the outer portion of the spray shows fewer droplets in the line of sight of the X-ray beam but with a similar EPL/d_l distribution, implying that the droplets in this region are sized similarly to the droplets toward the center of the spray.

Figure 6 presents a spray where there is swirl in the air portion of the nozzle with SR = 0.5. When Figure 6a is compared to Figure 5a, a shortening of the core region can be seen in the average plots. Additionally, a wider set of data was required for the SR = 0.5 condition because the swirled air increases the width of the spray. The PDF plots shown in Figure 6c, down the center of the spray, show that the values shift in a similar way towards zero like SR = 0 but do so much closer to the nozzle. Unlike in the condition where SR = 0, the SR = 0.5 condition does not have a converging region before it spreads. In Figure 6c the outermost data point that is near the nozzle exit shows that liquid is present in this region meaning that the spray has widened by $x/d_l = 0.026$, where the scan is taken. The bottom portion of the PDF plots shows a spray that is distributed with small EPL/d_l measurements which corresponds to small droplets.

Figure 7 shows a spray with a SR = 1. The PDF plots in Figure 7c show that the spray has no zero values just below the nozzle exit, in the center of the spray, consistent to the results from Figure 6c. However, comparing Figures 5-7 shows that the EPL/d_i distribution increases as SR increases. Additionally, the plots that are nearest the nozzle but on the outside edge show that as SR increases, the width of the spray very near the nozzle increases as there are successively less zero values with increasing SR. Unlike the condition where SR = 0 but similar to the condition where SR = 0.5, the condition with SR = 1 does not show a narrowing of the spray before it widens. A comparison of Figures 5c, 6c, and 7c show that as SR changes from 0 to 0.5 to 1, the values shift toward zero closest to the nozzle in Figure 6c, not as close in Figure 7c, and the furthest from the nozzle in Figure c. This is indicative of larger droplets existing in the condition where SR = 1.

An outline of the core region can be defined from the PDF plots as the region where values that fall into the 0.0

to 0.0255 EPL/d_l range makeup less than 5% of the total instances. When SR = 0, this region ranges from -1 to 1 at $y/d_l = 0.026$ and is narrower than -0.5 to 0.5 at $y/d_l = 0.714$ but is still present. When SR = 0.5, the core region ranges from -1 to 1 at $y/d_l = 0.026$ and from -1 to 1 at $y/d_l = 0.714$. When SR = 1, the core region ranges from -1 to 1 at $y/d_l = 0.026$, from -1 to 1 at $y/d_l = 0.714$, and is narrower than -0.5 to 0.5 at $y/d_l = 1.190$. However, because of the relatively large steps in these focused beam radiographs, the precise outline of the core cannot be determined from the data presented. This shortcoming is not a function of focused beam radiographs, just a result of this data collection cycle.

Summary and Conclusions

Maps of the average EPL from focused beam radiography provide visual insight into the location of the core and are used to visualize the width of the spray. Maps of the standard deviation show high values on the edges and lower portion of the core, corresponding to oscillations and shedding, respectively. Measures of the skewness and kurtosis both provide information about the width of the spray at various downstream locations but have not been found to provide additional insight into the physical properties that define the spray. The combination of these maps shows that the condition with SR = 0 has the longest core length, narrowest spray, and a large path length fluctuations around the core. The condition with SR = 0.5 has the shortest core, widest spray, and fewer fluctuations around the core. The condition with SR = 1 has a core length that is between SR = 0 and SR = 0.5, a spray width that is between SR = 0 and SR = 0.5, and path length fluctuations that are also between the conditions with SR = 0 and SR = 0.5.

Plots of the PDF of focused beam data points for conditions with varying SR show how adding swirl increases the width of the spray very near the nozzle. The condition with no swirl exhibits necking before widening but the conditions with swirl do not. The EPL distribution is consistent across the scan for all three conditions at $y/d_l = 0.714$ (the scan furthest from the nozzle). The portion of the spray that is furthest from the nozzle for the condition with SR = 0.5 exhibits EPL measurements that are closer to zero than the other conditions, providing evidence that the condition has small droplets in the region.

The wider distribution and smaller droplets that are created by increasing the portion of air that is swirled are advantageous for many spray systems. However, if the swirl ratio is increased too much, the droplets become larger, losing the advantage that was initially gained by increasing the swirl ratio. Because the total gas flow rate is kept constant throughout testing, the energy input is independent of SR. Spray properties can then be controlled based on the requirements of a particular system, without expending excess energy, which is advantageous for may spray systems.

Acknowledgments

This work was sponsored by the Office of Naval Research (ONR) as part of the Multidisciplinary University Research Initiatives (MURI) Program, under grant number N00014-16-1-2617. The views and conclusions contained herein are those of the authors only and should not be interpreted as representing those of ONR, the U.S. Navy or the U.S. Government.

This work was performed at the 7-BM beamline of the Advanced Photon Source, a U.S. Department of Energy (DOE) Office of Science User Facility operated for the DOE Office of Science by Argonne National Laboratory under Contract No. DE-AC02-06CH11357.

References

1. Lasheras, J. C., and Hopfinger, E. J., "Liquid jet instability and atomization in a coaxial gas stream", *Annual Review of Fluid Mechanics*, *32*(1), pp. 275-308, 2000.
2. Ofner, B., "Phase Doppler anemometry," *Optical Measurements: Techniques and Applications*, Springer, pp. 139-152, 1993.
3. Raffel, M., Willert, C. E., and Kompenhas, J., *Particle Image Velocimetry: A Practical Guide.*, Springer, 1998.
4. Caterjón García, R., Casterjón Pita, J. R., Martin, G. D., and Hutchings, I. M., "The shadowgraph imaging technique and its modern application to fluid jets and drops," *Revista Mexicana de Fisica*, 573: pp. 266-275, 2011.
5. Heindel, T. J., "X-ray imaging techniques to quantify spray characteristics in the near field," *Atomization and Sprays*, 28(11), pp. 1029-1059, 2018.
6. MacPhee, A. G., Tate, M. W., Powell, C. F., Yue, Y., Renzi, M. J., Ercan, A., and Gruner, S. M. , "X-ray imaging of shock waves generated by high-pressure fuel sprays," *Science*, *295*(5558), pp. 1261-1263, 2002.
7. Kastengren, A., and Powell, C. F., "Spray density measurements using X-ray radiography," *Proceedings of the Institution of Mechanical Engineers, Part D: Journal of Automobile Engineering*, 221(6), pp. 653-662, 2007.
8. Hopfinger, E. J., and Lasheras, J. C., "Explosive breakup of a liquid jet by a swirling coaxial gas jet," *Physics of Fluids*, *8*(7), pp. 1696-1698, 1996.
9. Kastengren, A., Powell, C. F., Arms, D., Dufresne, E. M., Gibson, H., and Wang, J.. "The 7BM beamline at the APS: a facility for time-resolved fluid dynamics measurements," *Journal of Synchrotron Radiation*, *19*(4), 654-657, 2012.
10. Hussain, A. K. M. F., and Ramjee, V., "Effects of the axisymmetric contraction shape on incompressible

turbulent flow," *Journal of Fluids Engineering*, 98(1), 58-68, 1976.

11. Lightfoot, M. D., Schumaker, S. A., Danczyk, S. A., and Kastengren, A. L., *Core length and spray width measurements in shear coaxial rocket injectors from X-ray radiograph Measurements* (No. AFRL-RQ-ED-TP-2015-115). Air Force Research Lab, Edwards AFB, CA, Aerospace Systems Directorate, 2015.
12. Li, D., Bothell, J. K., Morgan, T. B., Heindel, T, J., Aliseda, A., Machicoane, N., and Kastengren, A. L., "High-speed X-ray imaging of an airblast atomizer at the nozzle exit," *7th Annual Meeting of the Advanced Physical Society Division of Fluid Dynamics*, Denver, Colorado, November 19-21, 2017.

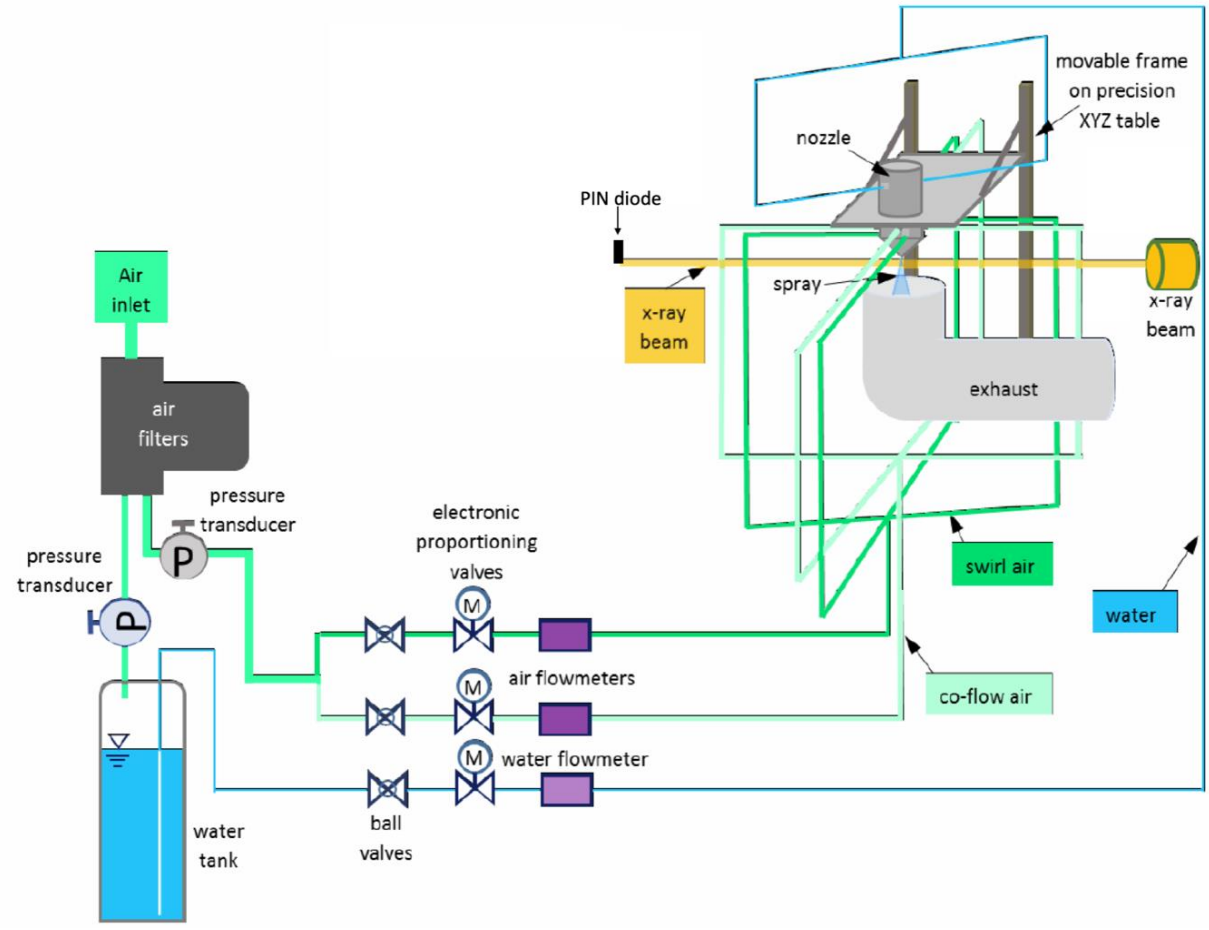

Figure 1. Schematic of the Advanced Photon Source (APS) experimental setup.

(a) 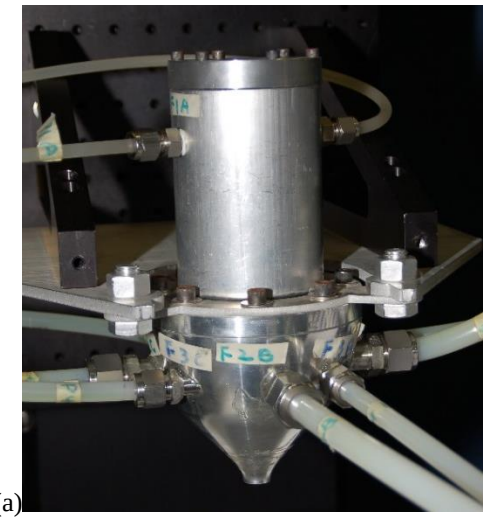 (b) 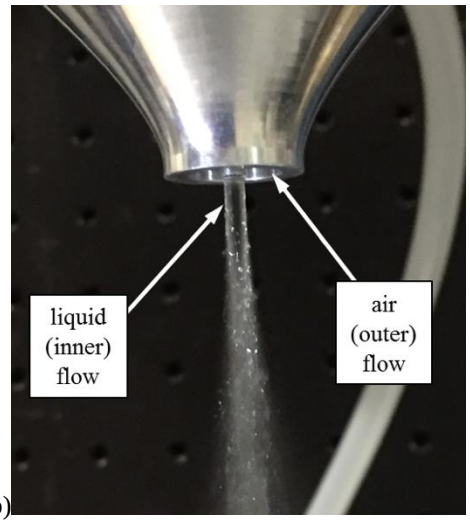

Figure 2. The airblast atomizer used in the experiments: (a) the water and air inlets and (b) a close-up of the nozzle exit.

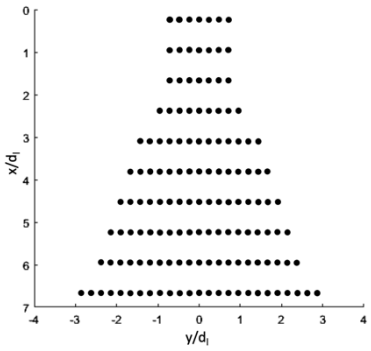

Figure 3. Data point locations of focused beam radiographs for the condition where $Q_l = 0.099$, $Q_g = 150$, SR = 0.

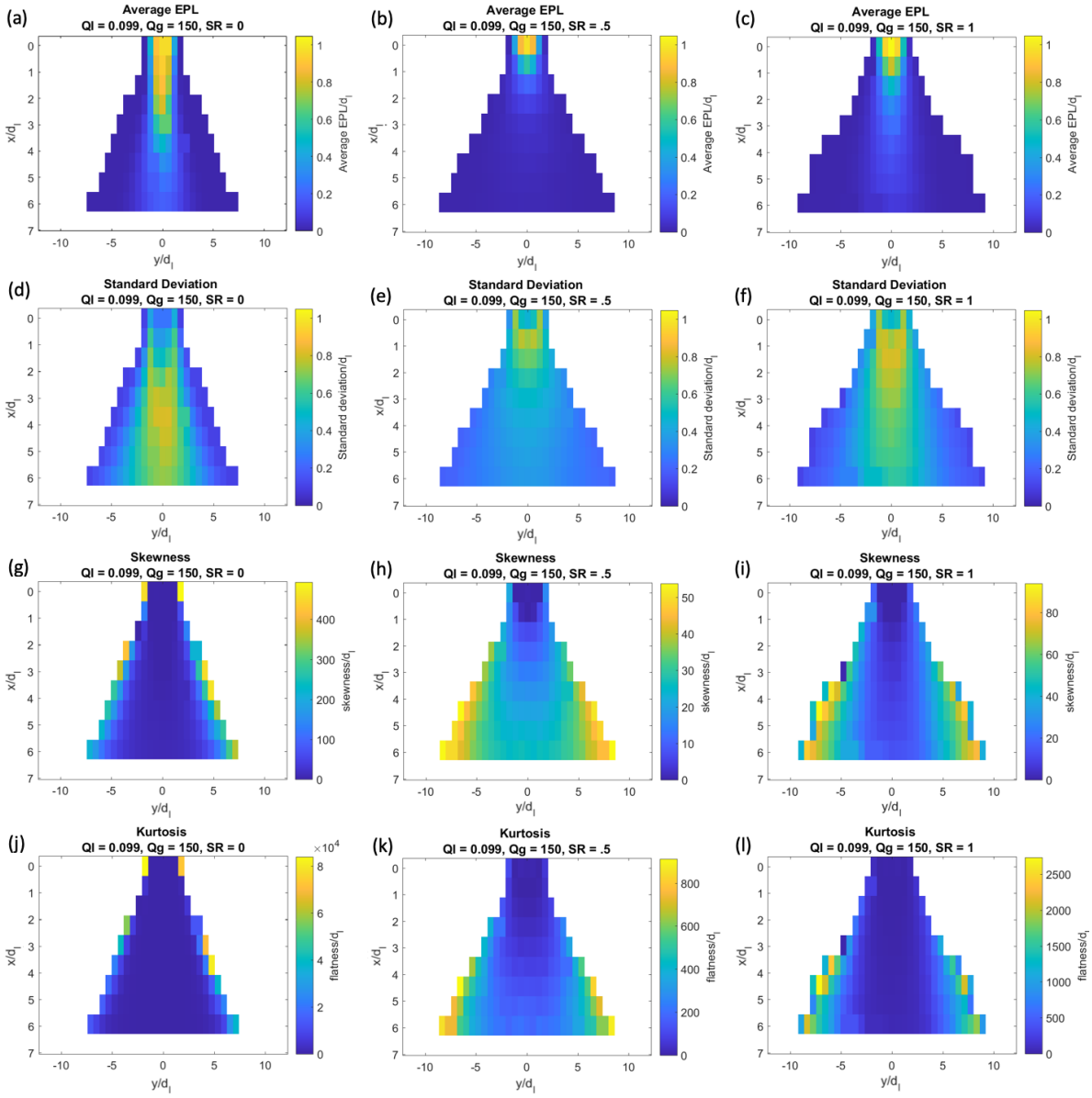

Figure 4. Comparison of effective path length (EPL) moments of distribution for sprays with varying swirl ratio (SR). Liquid flow rate, Q_l = 0.099 LPM and total gas flow rate, Q_g = 150 LPM with Re_l = 1,100 and Re_g = 21,200 for all conditions.

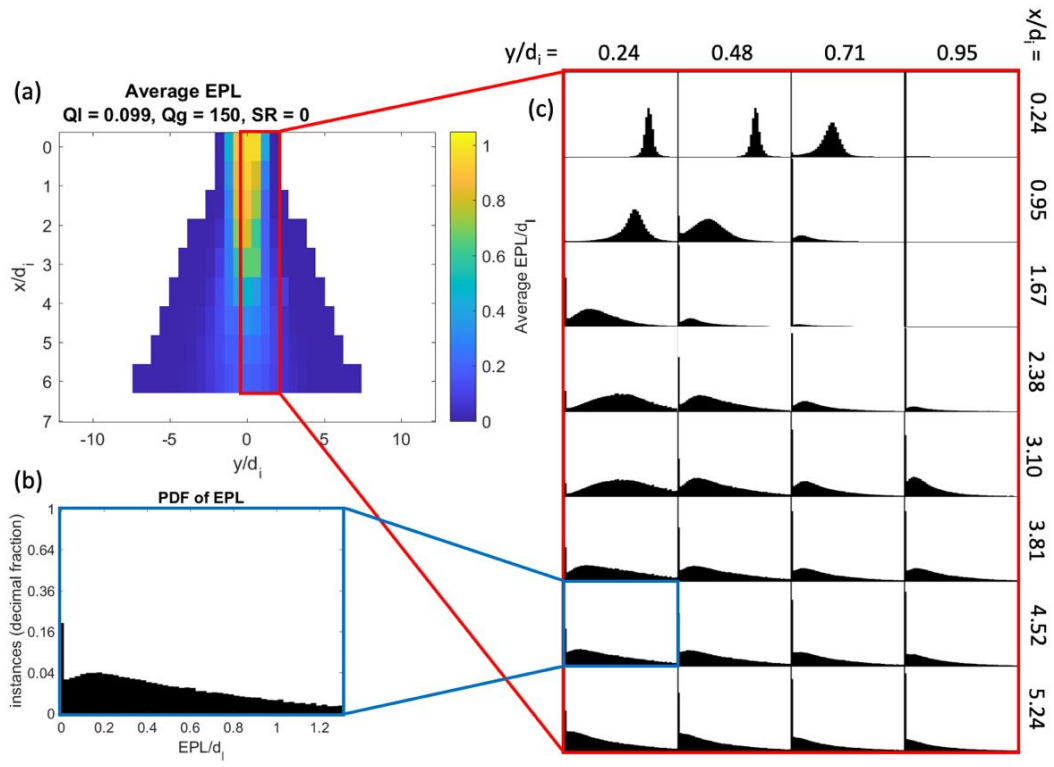

Figure 5. Condition with liquid flow rate, Q_l = 0.099 LPM; gas flow rate, Q_g = 150 LPM with Re_l = 1,100 and Re_g = 21,200; swirl ratio SR = 0. (a) Map of average effective path length, EPL, nondimensionalized with d_l. (b) Probability density function (PDF) of time-resolved EPL measurements with axis labels. (c) PDF of EPL plots for boxed regions in (a) with all axes identical to those in (b)

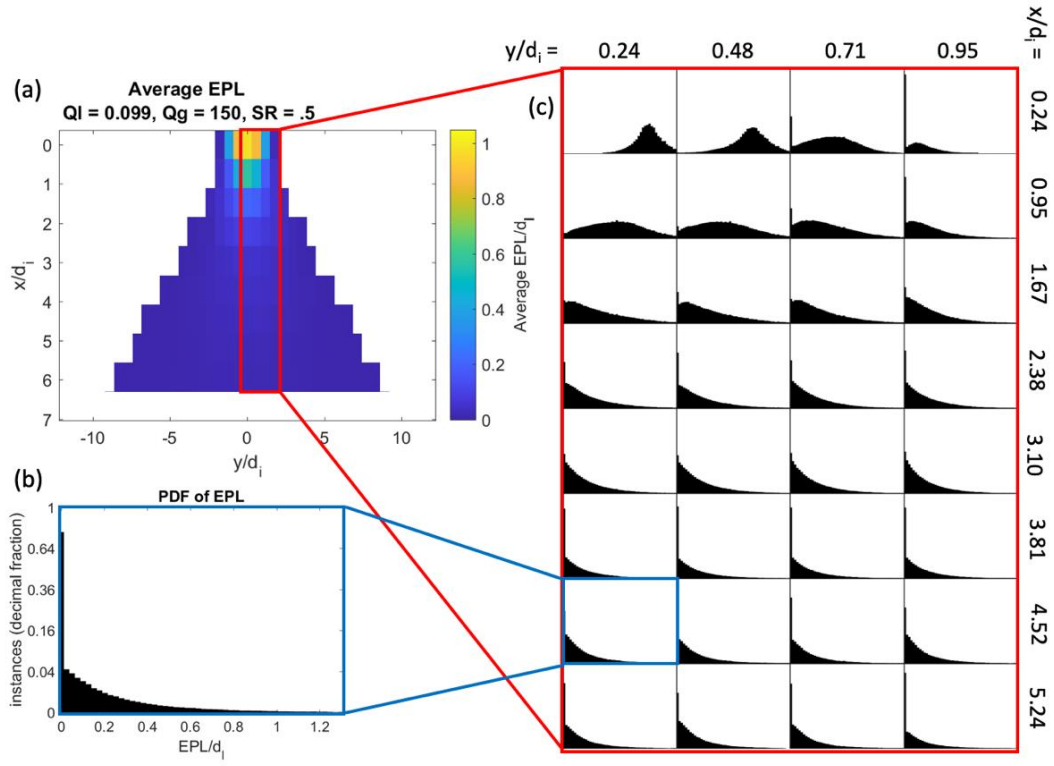

Figure 6. Condition with liquid flow rate, Q_l = 0.099 LPM; gas flow rate, Q_g = 150 LPM with Re_l = 1,100 and Re_g = 21,200; swirl ratio SR = 0.5. (a) Map of average effective path length, EPL, nondimensionalized with d_l. (b) Probability density function (PDF) of time-resolved EPL measurements with axis labels. (c) PDF of EPL plots for boxed regions in (a) with all axes identical to those in (b).

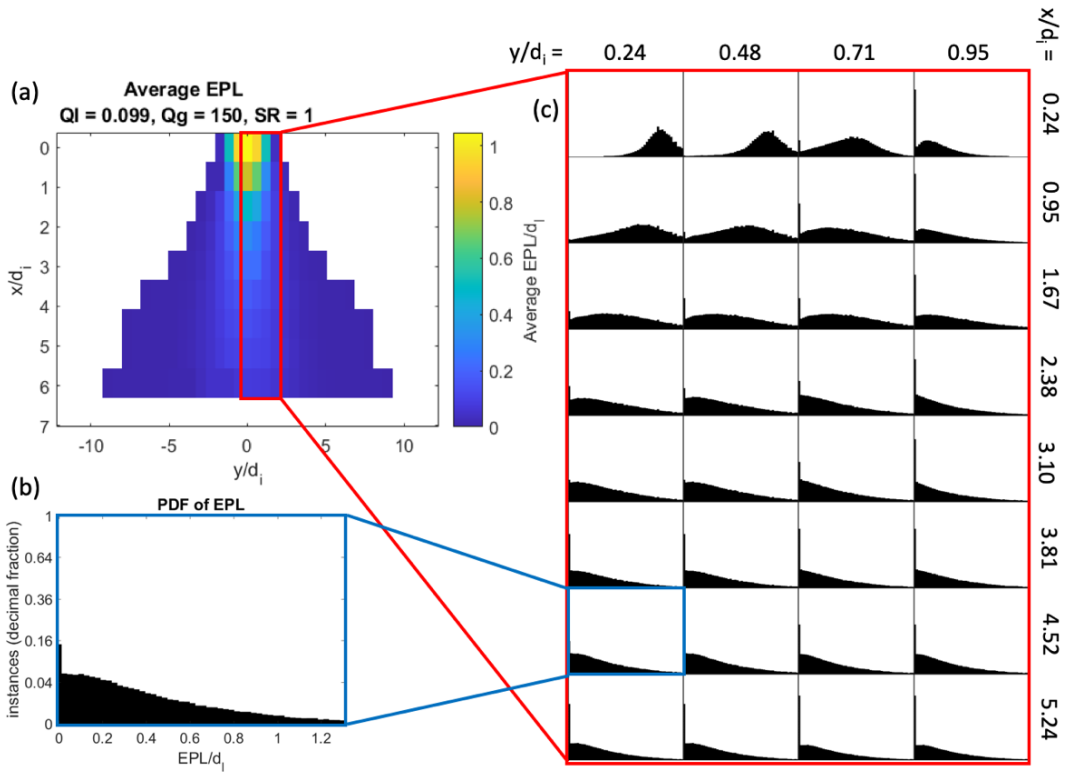

Figure 7. Condition with liquid flow rate, Q_l = 0.099 LPM; gas flow rate, Q_g = 150 LPM with Re_l = 1,100 and Re_g = 21,200; swirl ratio SR = 1. (a) Map of average effective path length, EPL, nondimensionalized with d_l. (b) Probability density function (PDF) of time-resolved EPL measurements with axis labels. (c) PDF of EPL plots for boxed regions in (a) with all axes identical to those in (b).